Time-domain diffuse optical tomography using silicon photomultipliers: feasibility study

Laura Di Sieno, Judy Zouaoui, Lionel Hervé, Antonio Pifferi, Andrea Farina, Edoardo Martinenghi, Jacques Derouard, Jean-Marc Dinten, Alberto Dalla Mora

Journal of Biomedical Optics

BiomedicalOptics.SPIEDigitalLibrary.org

Time-domain diffuse optical tomography using silicon photomultipliers: feasibility study

Laura Di Sieno
Judy Zouaoui
Lionel Hervé
Antonio Pifferi
Andrea Farina
Edoardo Martinenghi
Jacques Derouard
Jean-Marc Dinten
Alberto Dalla Mora

Laura Di Sieno, Judy Zouaoui, Lionel Hervé, Antonio Pifferi, Andrea Farina, Edoardo Martinenghi, Jacques Derouard, Jean-Marc Dinten, Alberto Dalla Mora, "Time-domain diffuse optical tomography using silicon photomultipliers: feasibility study," *J. Biomed. Opt.* **21**(11), 116002 (2016), doi: 10.1117/1.JBO.21.11.116002.

Time-domain diffuse optical tomography using silicon photomultipliers: feasibility study

Laura Di Sieno,[a,*] Judy Zouaoui,[b,c] Lionel Hervé,[b,c] Antonio Pifferi,[a,d] Andrea Farina,[d] Edoardo Martinenghi,[a] Jacques Derouard,[e] Jean-Marc Dinten,[b,c] and Alberto Dalla Mora[a]
[a]Politecnico di Milano, Dipartimento di Fisica, Piazza Leonardo da Vinci 32, Milano 20133, Italy
[b]Université Grenoble Alpes, CEA, Minatec Campus, 17 rue des Martyrs, 38054 Grenoble Cedex 9, France
[c]CEA, LETI, MINATEC Campus, 17 rue des Martyrs, Grenoble 38054, France
[d]Istituto di Fotonica e Nanotecnologie, Consiglio Nazionale delle Ricerche, Piazza Leonardo da Vinci 32, Milano 20133, Italy
[e]Université Grenoble Alpes, Laboratoire Interdisciplinaire de Physique (LIPhy), Pole Phitem, CS 40 700, 38058 Grenoble Cedex 9, France

Abstract. Silicon photomultipliers (SiPMs) have been very recently introduced as the most promising detectors in the field of diffuse optics, in particular due to the inherent low cost and large active area. We also demonstrate the suitability of SiPMs for time-domain diffuse optical tomography (DOT). The study is based on both simulations and experimental measurements. Results clearly show excellent performances in terms of spatial localization of an absorbing perturbation, thus opening the way to the use of SiPMs for DOT, with the possibility to conceive a new generation of low-cost and reliable multichannel tomographic systems. [DOI: 10.1117/1.JBO.21.11.116002]

Keywords: time-domain diffuse optics; diffuse optical tomography; silicon photomultipliers; time-correlated single-photon counting.
Paper 160476R received Jul. 7, 2016; accepted for publication Sep. 21, 2016; published online Nov. 3, 2016.

1 Introduction

Diffuse optical tomography (DOT) is an attractive noninvasive imaging technique that allows three-dimensional (3-D) volumetric reconstructions of optical properties within highly scattering media (e.g., biological tissues) down to a depth of few centimeters. Typically, visible and/or near-infrared light is shined/detected due to proper arrangements of many (e.g., few tens) injection and collection points.[1,2] DOT is useful for plenty of biomedical applications from neurology to oncology since optical absorption and scattering are, respectively, linked to chemical composition and microstructure of the investigated tissue.[1–6]

Depending on the thickness and geometry of the tissue under investigation, either transmittance (sources and detectors placed on opposite sides of the medium) or reflectance (sources and detectors placed on the same side at a given distance) approaches can be employed. However, the adoption of a reflectance configuration is, in most cases, mandatory owing that many regions of the human body are not accessible using a transmittance approach.

Three different measurement strategies can be employed since sources and detectors can be operated in three different domains: (1) continuous wave (CW), (2) frequency-domain (FD), and (3) time-domain (TD). The CW regime is the simplest one in terms of instrumentation, but the information content brought by one single measurement is poor. Indeed, it does not allow disentangling absorption from scattering contributions while this is, in principle, feasible in both FD and TD techniques.[2] However, only the TD approach has the added advantage of encoding different average penetration depths in the photon arrival time.[7,8] Therefore, a time-gated analysis[9] and/or detection[10,11] of the reflectance curve allows one to separate information coming from different layers of the investigated medium. The use of the photon arrival time as an additional information to differently weight spatial regions explored by the photons also leads to ideally better image quality with respect to other techniques,[12] as well as to lower dependence on moving artifacts.

An effective analysis of the reflectance TD curve can be achieved using the Mellin–Laplace transform (MLT).[13] Indeed, this approach permits, on one hand, one to achieve a variable time-windowing of the diffusion curve to fully take advantage of the information content of TD measurements. On the other hand, due to the windowing of the curves, it reduces the amount of information to be processed, thus reducing calculation steps and processing time.

Unfortunately, the widespread adoption of TD technique for DOT is mainly hampered by both overall cost and dimension of the system, being based on components much more complex than those required for CW instruments.[14,15] During the last two decades, picosecond pulsed lasers, time-resolved single-photon detectors, and time-tagging electronics have experienced considerable advancements, but the state-of-the-art TD-DOT systems like MONSTIR[16,17] and other instruments[18,19] are still large rack-based systems, limiting somewhat a widespread clinical adoption. In particular, since DOT requires a large number of detection points (e.g., few tens), the main bottleneck is still represented by the use of expensive, bulky, and delicate photocathode-based vacuum tubes like photomultiplier tubes (PMTs) or, more recently, hybrid PMTs.[20]

The unmet need for cost-effective and rugged detectors forced the interest of the scientific community toward microelectronic devices like single-photon avalanche diodes (SPADs).[21,22] Yet, their performance in diffuse optics systems is often unsatisfactory due to the small active area (few tens of micrometers in diameter) that affects the collection efficiency of diffused light. To cope with this limitation, SPADs require the use of lasers with high average power and, also, proper solutions for reducing

*Address all correspondence to: Laura Di Sieno, E-mail: laura.disieno@polimi.it

the light power density so as to match the maximum permissible exposure for skin.[23]

Very recently, silicon photomultipliers (SiPMs) were introduced in TD diffuse optics.[24] These promising detectors are inexpensive and rugged, they do not require complex front-end circuits, and they feature wide active areas of few square millimeters, thus permitting to maximize the photon collection. Essentially, they bring together the advantages of vacuum tubes and microelectronics detectors.

After initial positive results in proof-of-concept studies,[25,26] SiPM started to be integrated into compact and easy-to-operate detection modules[27] and to replace traditional PMTs in systems designed for clinical use.[28,29] Still, the state-of-the-art for SiPM technology is not yet fully miniaturized, but due to the possibility to integrate into a single silicon chip in both detectors and ancillary electronic circuits,[30,31] SiPMs represent the most attractive technology for the next-generation of DOT systems. Therefore, the demonstration of SiPM suitability also for TD-DOT could open the way to novel immediate perspectives due to the possibility to conceive low-cost and reliable multichannel systems.

Even if SiPMs have already been validated for diffuse optics in general, their suitability also for DOT is not straightforward. Indeed, as highlighted in Ref. 32, the present generation of SiPMs employed as time-resolved single-photon detectors is affected by some limitations. The most critical one is the presence of a slow exponential decaying tail (known as "diffusion tail" being due to the diffusion of photogenerated carriers inside the detector) in the single-photon response shape of the device. This tail is characterized by a few nanoseconds decaying time-constant starting 1 to 2 decades below the response peak.[32] As demonstrated in Ref. 33, the tails in the response function can seriously affect the performance of the device in TD diffuse optics in general, possibly preventing the capability to detect and localize absorption perturbations within the diffusive medium. Additionally, this long tail limits the dynamic range of the detector response function to about 2 orders of magnitude,[32] thus possibly affecting DOT reconstructions due to the reduced range suitable for data analysis.[34] As reported in Ref. 32, SiPMs are also characterized by high noise background (up to few hundred thousand counts per second, depending on the operating conditions), which limits the maximum number of photons per second that can be detected to avoid pile-up effects in TD acquisitions using time-correlated single-photon counting (TCSPC) systems,[20] and also, the minimum photon bunch, which can be extracted out of the noise. As a final concern, the temporal stability of the detector response function has to be carefully considered in TD-DOT systems. Indeed, DOT can involve long acquisition times, in particular, when tomographic reconstructions are obtained by scanning the tissue surface instead of using a multichannel system.[10]

The aim of this paper is to address these issues and demonstrate the suitability of SiPMs for optical tomography in the TD. In particular, we have studied on tissue-mimicking heterogeneous phantoms (using absorbing inclusions at different depths), the sensitivity of SiPMs to deep perturbations into the medium and their capability to properly localize and reconstruct buried inclusions. The paper is organized as follows: in Sec. 2, we describe the experimental setup and the signal analysis technique; Sec. 3 deals with simulations and phantom measurements; finally, in Sec. 4, we summarize the main results of the paper and discuss future perspectives.

2 Material and Methods

2.1 *Experimental Setup*

Figure 1 reports the setup used for the experiments. The light source was a mode-locked laser (Fianium Ltd., United Kingdom) providing optical pulses [duration: 26-ps full-width at half maximum (FWHM)] at 820 nm at the repetition rate of 40 MHz. The light passed through a variable optical attenuator and was then injected into the sample through an optical fiber [core diameter: 200 μm; numerical aperture (NA): 0.22; Lightech srl, Italy]. The photons re-emitted from the sample were then collected at two different points by means of two optical fibers (core diameter: 1 mm, NA: 0.37; Thorlabs Gmbh, Germany). We decided to use two detection points so as to increase the quality of the reconstructed image by acquiring data from multiple points of view. The distance between injection and collection fibers was set to 30 mm. The light exiting from each collection fiber was then imaged onto a SiPM detector by a set of two lenses (achromatic doublets lens, focal length: 30 mm) providing a 1× magnification.

Each module embeds a 1 mm^2 active area SiPM (C30742-11-050-T1, Excelitas Technologies, Canada) and all the required electronic circuits for sensing and amplifying the avalanche signal and yielding the pulse synchronous with the avalanche. Additionally, the module hosts a thermoelectric cooler controller board, which is set to keep the detector at about 15°C. This value represents the best compromise to limit both primary dark count rate and afterpulsing (i.e., noise contribution due to charge carriers trapped during the avalanche ignition). For further details about the SiPM module design and characterization, see Ref. 27. Each SiPM module was then coupled to a TCSPC board (SPC-130, Becker&Hickl GmbH, Germany) to provide the start signal for time-stamp generation. The stop pulse was given to both TCSPC boards by the "synchronization" output of the laser.

To acquire the instrument response function (IRF) of the system, we directly faced the source fiber and one detector fiber at a time, putting a thin Teflon layer in-between to ensure the isotropic illumination of the latter. The IRFs obtained for a 10-s measurement time and after the subtraction of the mean value of

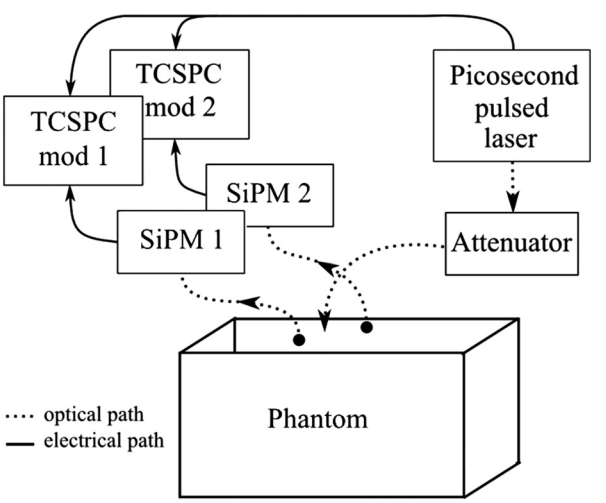

Fig. 1 Experimental setup: a pulsed laser light is attenuated and shined onto a phantom through an optical fiber. The backscattered photons are detected by the two SiPM modules, which provide the start signal to the TCSPC boards, while the stop one is given by the laser.

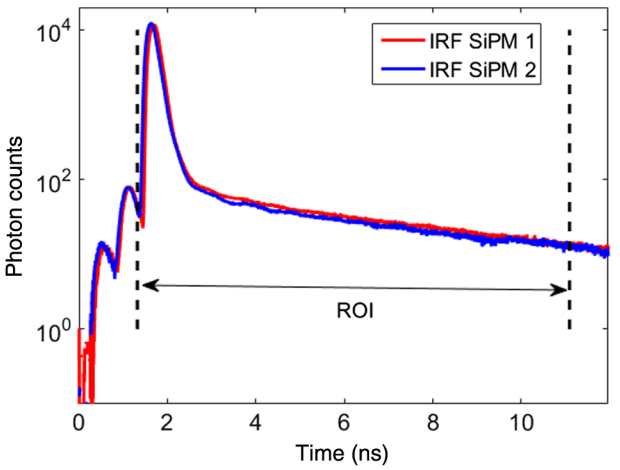

Fig. 2 IRF recorded with both SiPM modules (constant background subtracted). The region of interest (ROI) is the portion of the curve used for simulations.

the background noise for both SiPM modules are reported in Fig. 2. The peak timing jitter (FWHM) is around 260 ps for both detectors (262 ps for module 1 and 255 ps for module 2) while the tail with a long time constant (~3 ns) starts 2.5 decades below the peak, in agreement with Ref. 32.

The homogeneous liquid phantom was a water dilution of black Indian ink (which acts as an absorber) and Intralipid (providing scattering property). The proportion of the components were chosen so as to have an absorption coefficient (μ_a) of 0.07 cm^{-1} and a reduced scattering one (μ_s') of 12 cm^{-1} at 820 nm.

As an absorbing inhomogeneity within the homogeneous medium, we used five totally absorbing inclusions [black cylinders made of black polyvinyl chloride (PVC)] of different volumes. As reported in previous studies,[35,36] small totally absorbing objects properly reproduce realistic absorption inhomogeneity in a reliable and reproducible way and for a wide range of applicability. In particular, for a given μ_s' background, it is possible to identify a whole equivalence class of absorbing perturbations, with different size and shape, which yield the same temporal perturbation for any choice of geometry (e.g., reflectance, transmittance, source–detector distance), position of the object within the medium, and background absorption. Each equivalence class also contains a totally absorbing object whose volume [equivalent black volume (EBV)] can be taken as representative of the whole class. Some breaking of the equivalence are observed only when black object has a very small volume ($\leq$50 mm^3) and the object is quite close (depth $\leq$10 mm) either to the source or to the detector. The black inclusions we used in this work were cylinders with height equal to the diameter with values of 3.2, 4, 5, 6.8, 8.6 mm, a volume EBV = 25, 50, 100, 250, 500 mm^3, and corresponding to an equivalent $\Delta\mu_a = 0.056$, 0.087, 0.15, 0.37 and 0.94 cm^{-1} for a 1 cm^3 volume, respectively.[36] In this paper, the inclusions will be named as "inclusion 1, 2, 3, 4, or 5" depending on their volume (e.g., we will refer to the 100 mm^3 as "inclusion 3"). For what concerns data presented in the following section, in most cases, there is negligible discrepancy in the equivalence relation: only in two cases (EBV = 25, 50 mm^3, with depth = 10 mm), some 10% to 20% discrepancy in the amount of perturbation as compared to the equivalent realistic inhomogeneity is observed.[36]

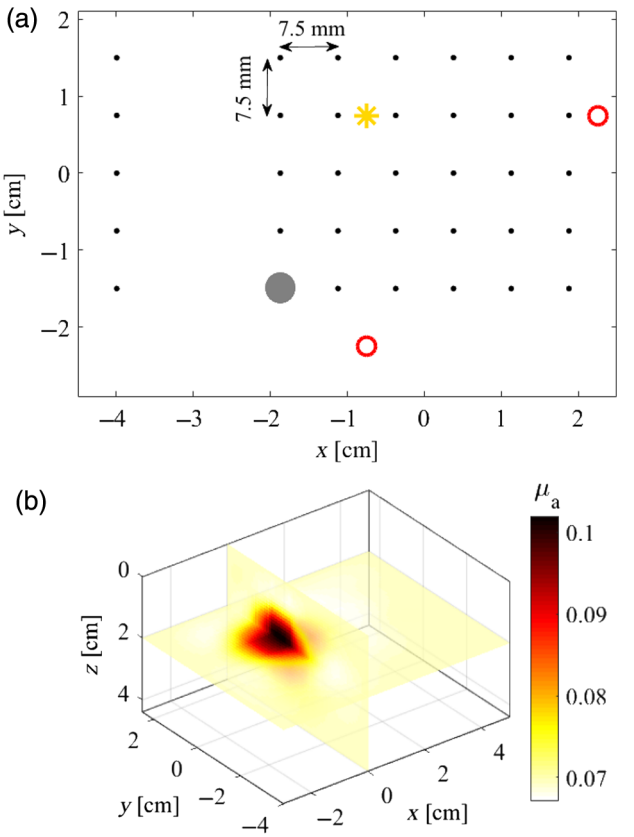

Fig. 3 (a) Geometry of the scan in the $x - y$ plane: injection and collection fibers (yellow star and red open circle, respectively) are fixed while the inclusion (gray filled circle) was moved in the different positions (black dots). (b) Example of a 3-D $\mu_a$reconstruction of the inclusion at 20-mm depth using simulation data.

Since multiple measurements are needed to obtain a tomographic reconstruction during measurements, the injection and collection fibers [represented, respectively, as yellow star and open red circles in Fig. 3(a)] were kept fixed while the inclusion was moved. This strategy was selected in order to avoid possible artifacts due to the movement of fibers, which were instead bound to the phantom tank using a black PVC plate in which holes for fiber tips were drilled. Using a motorized three-axes translation stage, the inclusion was moved over an area of 3.75 × 3 cm^2 at steps of 7.5 mm in both x and y directions [scan area: from −18.7 to 18.8 mm and from −15 mm to 15 mm for x and y direction, respectively]. For each inclusion position [small black dots in Fig. 3(a)], we acquired the signal for 15 s (15 repetitions of 1 s each). As reference measurement, for each line, we moved the inclusion far enough ($x = -40$ mm) to consider its effect negligible.

For each perturbation, we first aligned the inclusion at 7.5 mm from the injection fiber in both x and y directions, and this point was set as origin for the scanning coordinates system. This choice was done to obtain a scanning area not centered to the inclusion position, thus being able to disentangle the reconstruction of the inclusion from possible artifacts arising in the center of the image.

Scans of all the inclusions in the $x - y$ plane were done at different depths (where "depth" refers to the distance from the surface of the phantom to the center of the inclusion) ranging from 10 mm up to 20 mm at step of 5 mm. Also, only for

Table 1 Recovered value of x, y and depth localization and value of quantified $\Delta\mu_a$ computed for both simulations and experiments for all inclusions. "Sim ideal" corresponds to the simulations using the IRF of SPAD.

				x localization (expected: $x = 0$)		y localization (expected: $y = 0$)		Depth localization		Recovered $\Delta\mu_a$		
Inclusion	EBV (mm^3)	$\Delta\mu_a$ for 1 cm^3 (cm^{-1})	Depth (mm)	Sim (mm)	Exp (mm)	Sim (mm)	Exp (mm)	Sim (mm)	Exp (mm)	Sim ideal (cm^{-1})	Sim (cm^{-1})	Exp (cm^{-1})
1	25	0.056	10	0.21	1.41	−0.38	−0.36	11.4	11.3	0.031	0.031	0.053
			15	0.37	1.11	−0.26	−0.23	17.7	17.4	0.021	0.021	0.031
			20	0.16	0.86	−0.12	−1.01	20.9	19.8	0.013	0.012	0.014
2	50	0.087	10	0.23	1.67	−0.39	0.03	11.5	11.5	0.046	0.047	0.070
			15	0.24	1.40	−0.30	0.11	17.9	16.8	0.030	0.030	0.038
			20	0.27	1.23	−0.15	−0.51	21.0	19.8	0.018	0.018	0.019
3	100	0.150	10	0.24	1.98	−0.42	0.06	11.5	11.6	0.078	0.076	0.107
			15	0.28	1.68	−0.15	0.30	17.8	16.8	0.050	0.046	0.056
			20	0.11	1.43	−0.11	0.91	20.7	19.5	0.031	0.026	0.029
			25	−0.06	−0.90	−0.03	−1.95	22.7	21.4	0.012	0.009	0.012
			30	1.29	−0.31	0.40	−6.58	24.6	19.6	0.004	0.003	0.002
4	250	0.370	10	0.26	1.46	−0.38	0.07	11.8	11.4	0.145	0.147	0.177
			15	0.34	1.57	−0.26	0.41	17.5	16.2	0.085	0.086	0.085
			20	0.14	0.69	−0.21	1.02	20.4	19.9	0.048	0.045	0.045
5	500	0.940	10	0.23	1.12	−0.34	0.43	12.2	11.1	0.227	0.225	0.275
			15	0.34	1.16	−0.24	0.92	17.2	15.3	0.119	0.123	0.125
			20	0.20	1.04	−0.19	1.12	20.0	18.6	0.062	0.063	0.058

"inclusion 3," 25 and 30 mm depth scans were acquired in order to test the depth sensitivity of the setup. The depth was automatically changed using the motorized translation stage when a scan on the $x - y$ plane was finished.

2.2 *Data Analysis*

In the following, the diffusion approximation was used to model light propagation.[37] Data analysis was performed considering two sets of measurements $M^A_{sd}(t)$ and $M^B_{sd}(t)$, acquired on a reference medium A (homogeneous medium of known absorption μ_a^A) and on the unknown medium B (with unknown absorption μ_a^B, but estimated at iteration k by $\mu_a^{B(k)}$). As explained in Ref. 13, the reference measurement is needed to take into account the effect of the IRF. In the previous expression of measurements, t is the time, s is an index on the source position, and d is an index on a detector position. As in Ref. 13, we used the combination $Y_{sd}(t)$ obtained with these measurements and known Green's functions G^A of medium A and Green's functions $G^{B(k)}$ of estimated medium B at iteration k, which is linearly related to the absorption update $\delta\mu_a^{(k)} = \tilde{\mu}_a^B - \mu_a^{B(k)}$. Green's functions G are defined as solutions of the diffusion equation for a Dirac source. In the reported experiment, μ_s' was measured (12 cm^{-1}) and was not considered as an unknown parameter in the data analysis. After space discretization with finite volume method and time discretization with the MLTs,[13,38] we ended up with this system:

$$\begin{cases} Y_{sd}^{(p,n)(k)} = \sum\limits_{e+f=n} M_{sd}^{B(p,e)} \cdot G_{sd}^{A(p,f)} - M_{sd}^{A(p,e)} \cdot G_{sd}^{B(p,f)(k)} \\ Y_{sd}^{(p,n)(k)} \approx - \sum\limits_{i+j+l=n} M_{sd}^{A(p,i)} \cdot \sum\limits_{m} G_{s,m}^{B(p,j)(k)} \cdot \delta\mu_{a,m}^{(k)} \cdot G_{d,m}^{B(p,l)(k)} \end{cases} \tag{1}$$

where p is the MLT precision of analysis (a real positive value, set to 3 ns^{-1}, same as in Ref. 13), n is the MLT order (an integer number, here growing from 0 to 20). The space discretization was performed on a regular $80 \times 65 \times 45$ mm^3 mesh grid of the medium, partitioned in tetrahedra with 31119 nodes indexed by m. The unknown $\delta\mu_a^{(k)}$ was determined using a conjugate gradient method. Since Eq. (1) (bottom) is a development at the order 1 of μ_a, an iterative approach must be undertaken if accurate absorption determination is sought; therefore, we processed our reconstruction by step and updated the absorption $[\mu_a^{(k+1)} = \mu_a^{(k)} + \delta\mu_a^{(k)}]$ and the predicted Green's functions $(G^{B(k)})$ reported in Eq. (1) at each iteration k up to 10.

2.2.1 *Simulations*

To evaluate the performance of the system, we first carried out a simulation study in the same conditions (same geometry and same reconstruction method) as the described experiments. We generated simulated measurements by time-convoluting computed Green's functions (for each simulated phantom) and the experimental IRF of the SiPM (within the region of interest highlighted in Fig. 2) and by adding Poisson noise. We decided to consider only Poisson noise since it is the only unavoidable noise contribution.[39] Indeed, other sources of noise (e.g., laser power instability, thermal drifts, and so on) are dependent on the particular system being used. It is worth noting that a detailed simulation of the performance of this particular system is out of the scope of this paper. The scope of the presented simulations is to investigate whether or not SiPMs, with their distinctive IRF, can allow tomographic reconstructions. Therefore, simulations should represent the best results allowed by this technology. The simulated phantoms were composed of the same homogenous background medium as the experiment and the same perturbations: 1 cm^3 spheres with $\Delta\mu_a$ equivalent to those provided by the total absorbing inclusions we used for experiments. Figure 3(b) shows an example of a 3-D μ_a reconstruction result for an inclusion set at 20 mm depth obtained in simulation.

To ascertain whether the SiPM performances can alter the quantification capabilities of the system, we have also performed reconstructions on simulations using the IRF of a high-performance SPAD. Indeed, it can be considered as a state-of-the-art, quasi-ideal detector due to its fast response (FWHM timing jitter = 29 ps, diffusion tail time constant <100 ps[40]). Due to the narrow jitter of the SPAD detector, its contribution to the system jitter is expected to be negligible. Indeed, the main contribution to the system jitter is the dispersion introduced by 1-mm core optical fiber, whose value can be derived from the SiPM IRF since all other contributions (e.g., laser jitter, TCSPC card jitter, and so on) are known and can be considered negligible. We therefore considered a FWHM value of the SPAD-based IRF of 258 ps, which is about the average value of the IRF jitter reported in Sec. 2.1.

2.2.2 *Parameters of interest*

Data analysis of the 3-D reconstructions (coming both from simulations and measurements) was computed to extract spatial and absorption quantification information, as reported in Table 1. To get the values of spatial localization (x, y, and depth), the weighted centroids of each reconstructed inclusions were calculated on a delimited region defined by all values above a threshold of 50% of the absorption variation $\Delta\mu_a^{vol}$, where $\Delta\mu_a^{vol}$ is calculated by taking the average over a 1 cm^3 sphere at the expected depth of the inclusion. The expected values of the recovered x and y position are $x = 0$ and $y = 0$ for all depths.

3 Results and Discussion

3.1 *Simulations*

Figure 4 shows the reconstructed maps (in the $z - y$ and $x - y$ planes, first and second row, respectively) for the "inclusion 3" at depths ranging from 10 mm up to 30 mm (columns). The black circle reported in each map represents the volume of 1 cm^3 in which the absorption perturbation given by the inclusion is supposed to be. It is clearly noteworthy that in the $z - y$ plane, the position of the absorption perturbation is properly localized in depth till 25 mm, while for larger depths, it is reconstructed in a position shallower than the real one. On the other hand, in the $x - y$ plane, there is a proper localization of the inclusion at all depths. For both $z - y$ and $x - y$ slices at almost all depths, the reconstructed volume is larger than the expected 1 cm^3 and, more precisely, it progressively increases at higher depths. This is due to the fact that the information of deep inclusions is carried by photons with a long time-of-flight, thus providing a lower spatial resolution.[41]

With the aim to study the sensitivity to the amount of absorption perturbation, Fig. 5 reports the reconstructed maps (at a given depth: 15 mm) obtained using the whole set of totally absorbing objects. Regardless the volume, the position of the inclusion in both planes ($z - y$ and $x - y$) is precisely reconstructed (for values, see Table 1). In addition, we clearly see that as the real $\Delta\mu_a$ of the perturbation increases, the retrieved $\Delta\mu_a$ increases as well (even if the absolute value is lower than expected) while the reconstructed volume does not, as expected. Indeed, since the inclusions depth is the same, the spatial resolution of the system is expected to be the same.

From simulations, we can conclude that SiPMs are suitable for the tomographic reconstruction of even small absorption

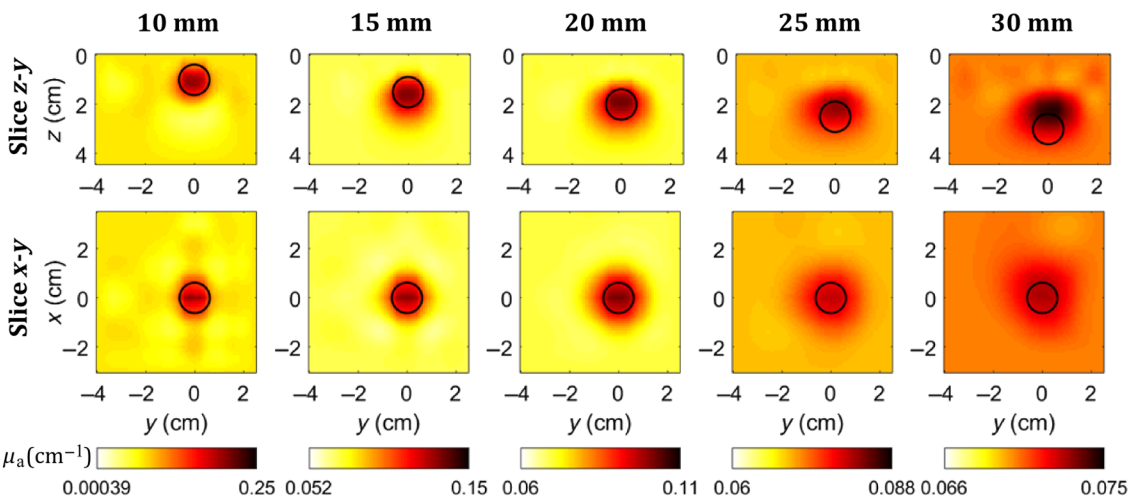

Fig. 4 Simulation: sections of 3-D reconstructions of a perturbation equivalent to "inclusion 3" at different depths.

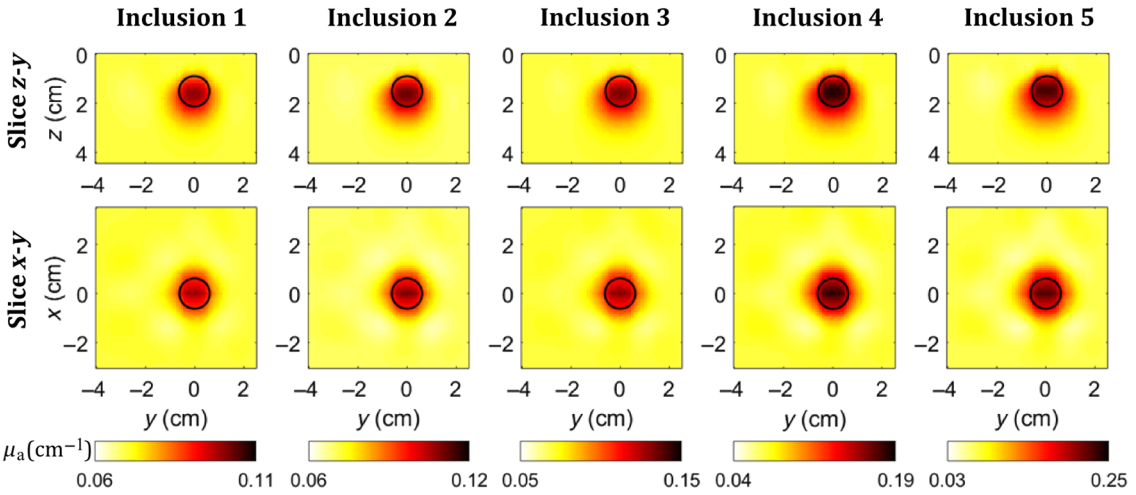

Fig. 5 Simulation: sections of 3-D reconstructions for perturbations equivalent to the five inclusions at 15-mm depth.

perturbations ($\Delta\mu_a = 0.056$ cm^{-1}) buried down to 20 mm (see Table 1), with good accuracy in terms of depth and lateral resolution. Indeed, for both x and y localization, the recovered position always differs of <0.5 mm from the expected one, whereas for the z axis, the relative error in depth localization is always <3 mm (for inclusion 2 at depth 15 mm, which corresponds to an error of 16%). By contrast, the absolute quantification of the perturbation is not accurate, and its accuracy decreases upon the increase of the inclusion's volume. However, the simulations done with the quasi-ideal detector reported in Table 1 clearly demonstrate that this lack in accuracy is not dependent on the peculiar features of the SiPM (e.g., slow diffusion tail), since similar results in quantification are recovered also using a state-of-the-art detector.

Due to the encouraging results obtained in the simulations, we have studied the suitability of the SiPM for TD-DOT with experimental measurements.

3.2 *Experimental Measurements*

The effect of the depth (ranging from 10 to 30 mm, columns) for "inclusion 3" in phantom measurements can be seen in Fig. 6, where the $z-y$ (first row) and $x-y$ (second row) maps are reported. Up to 25 mm depth, the spatial localization (depth and $x-y$) is comparable with simulations. For the 30-mm depth measurement, the perturbation is probably too low to properly detect the inclusion, thus resulting in an unsatisfactory localization of the perturbation. For all depths, there is a larger number of artifacts than in simulations, but this is most likely due to instabilities of the experimental system (e.g., laser instability, ageing of the phantom) that were not taken into account in simulations. In any case, it is worth noting that the current setup is able to reconstruct an equivalent absorbing perturbation of 0.15 cm^{-1} (for 1 cm^3 volume), which is buried down to 25 mm in depth. Those values are typical for biomedical applications (e.g., optical mammography or brain imaging) thus making the use of SiPMs a good solution in medical imaging.

To ascertain the sensitivity on the amount of absorption perturbation, Fig. 7 shows the $z-y$ and $x-y$ maps for the five inclusions at the same depth (15 mm). It is worth noting that all inclusions are properly reconstructed in terms of depth and $x-y$ position.

Concerning the quantification of the absorption perturbation for experimental measurements, it is similar to that obtained from simulations for both the absolute value and for the trend, showing a lower value of $\Delta\mu_a$ upon an increase of the depth.

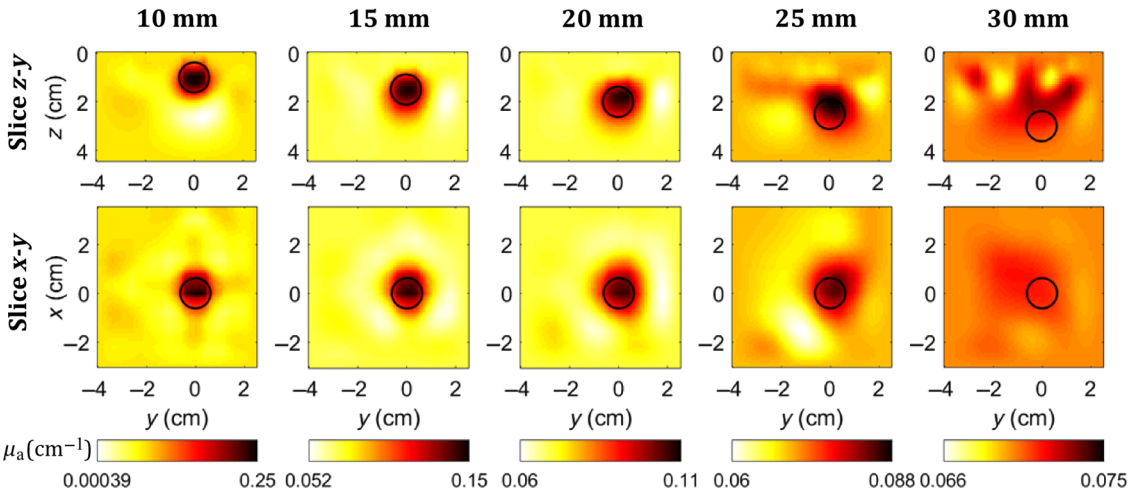

Fig. 6 Experiment: sections of 3-D reconstructions of the "inclusion 3" at different depths.

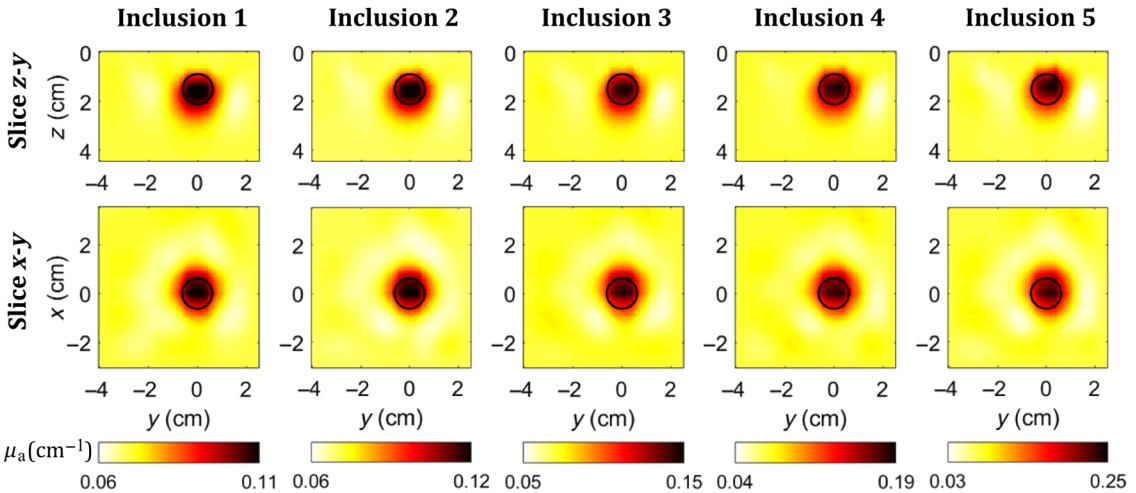

Fig. 7 Experiment: sections of 3-D reconstructions for the five inclusions at 15-mm depth.

As can be seen in Table 1, the depth localization is quite accurate for all depths with an error always lower than 2.5 mm (up to 20-mm depth) that corresponds to a maximum error of 17%. We can also notice that experiments and simulations show a good agreement with a discrepancy in the position of the inclusion, which is always lower than 2 mm for depths (except for 30 mm).

The retrieved coordinates of the x position of the inclusion recovered from the experiments seem to systematically differ by about 1 to 2 mm from the expected position. Maybe this is due to some systematic errors in the alignment of the inclusion in the experimental measurements. On the other hand, the y localization presents a slighter error (<1 mm) for both the simulation and the experimental data. To conclude, the error in the localization is small enough not to affect significantly the capability of the system to retrieve the position of an absorbing perturbation in a real application.

The "inclusion 3", set at a depth of 30 mm, produced a too low perturbation to be able to properly localize it not only in depth but also in the x and y directions. For this reason, we can state that the maximum depth of the inclusion allowing proper tomographic reconstruction is 25 mm.

Concerning the quantification capability on the retrieved $\Delta\mu_a$, measurements and simulations are usually in good agreement (see Table 1). The only exception is for inclusion 1 and 2 at a shallower depth, which could be partially ascribed to the deviation of the equivalence relations between EBV and the realistic $\Delta\mu_a$, which, for these particular cases, implies ~20% higher contrast for the black object in the experiments. On the other hand, there is a clear underestimation in the reconstructed $\Delta\mu_a$ upon increasing the depth. Since this trend is present also in simulations, we suppose that it is not possible to ascribe it to an experimental problem, but more to an issue connected with the model used for reconstruction. Indeed, as discussed in Sec. 3.1, simulations using an almost ideal detector (without long tail) are substantially in agreement with SiPM simulations. Thus, we can conclude that SiPM performances do not alter $\Delta\mu_a$ quantification capabilities as compared to a state-of-the-art detector.

The absolute quantification of the perturbation is a well-known problem in tomography[42] in particular for deep inhomogeneities. More comprehensive studies are needed to quantify this effect properly, identify the determinants, and try to improve quantitation. Surely, the decrease in retrieved μ_a for increasing depth is a concern when imaging complex structures since fluctuations in reconstruction due to shallower inhomogeneities can hinder deeper and attenuated structures. From the data in Table 1, this effect—for the background properties presented in this study ($\mu_a = 0.07$ cm^{-1}, $\mu_s' = 12$ cm^{-1})—is around a factor of 3 to 4 between a depth of 10 and 20 mm. Yet, this effect is compensated by the broadening of the reconstructed inhomogeneity, which implies that the overall impact of the deeper perturbation on the image is somehow augmented. In a different study, with conventional detectors, we have shown that fixing the size of the reconstructed inhomogeneity to the true value, as could be obtained through a coregistration with another imaging modality, completely solves the depth reduction in reconstructed μ_a.[43]

4 Conclusions

In this work, SiPMs are proposed as potentially revolutionary detectors for TD-DOT due to their unique features, bringing together the advantages of PMTs and SPADs. In particular, our aim was to validate their performance on heterogeneous phantoms to evaluate the impact of their inherent disadvantages: a slow tail and low dynamic range in the temporal response to single photons, a high background noise, and unknown stability for long measurement times in TCSPC applications. We performed a study based both on simulations (taking into account the true detector temporal response) and experiments in order to disentangle nonidealities of the employed system from the actual detector behavior.

We demonstrated from both points of view that SiPMs clearly allow one to detect perturbations of $\Delta\mu_a = 0.15$ cm^{-1} in a volume of 1 cm^3 down to 3 cm depth into a scattering medium featuring $\mu_a = 0.07$ cm^{-1} and $\mu_s' = 12$ cm^{-1} using a 3-cm inter-fiber distance. An excellent precision in lateral localization (better than 2 mm) is obtained down to a 2.5-cm depth, whereas depth localization is good up to 2 cm (better than 3 mm). Additionally, it is worth pointing out that with a perturbation placed at a depth of 2 cm, a lateral localization better than 1.5 mm and a depth localization better than 1.5 mm can be achieved with a large range of perturbation values, ranging from $\Delta\mu_a = 0.056$ cm^{-1} to $\Delta\mu_a = 0.94$ cm^{-1}. By contrast, the accuracy in quantification of the absolute value of the perturbation is much worst, with a strong underestimation of the retrieved $\Delta\mu_a$ upon increasing depth. Still, this effect is not

ascribed to the SiPMs since it is replicated in simulations also for a state-of-the-art, almost ideal detector. The problem of the absolute quantification in diffuse optics measurements is well known in the literature[42] and a dedicated effort is needed to properly address this issue, which is out of the scope of this work. Preliminary results show that this issue is due to the physics of diffuse optics and the retrieval algorithm and not to the specific experimental implementation.[43]

The demonstration of SiPM suitability for TD-DOT opens now the way to interesting perspectives. In this work, we made use of two custom-made detection modules based on SiPMs. As reported in Ref. 27, the overall dimensions of each module is 5 cm × 4 cm × 10 cm while the cost in terms of components is around 1000 €. This solution allowed us to get rid of thermal drift and electromagnetic interferences and to maintain high timing resolution due to the high-performance radiofrequency electronics that can be hosted inside such detection modules.[27] However, with the aim to conceive multichannel systems, most of the electronics presently hosted into the module can be shared between different channels (e.g., power supply generators and high-voltage circuitry for SiPM biasing), thus further lowering sizes and costs even with the state-of-the-art technology. More farseeing, fully integrated devices embedding the detector, its ancillary electronics, and also the TCSPC circuitry represent an incredible possibility to fabricate detection chains with millimetric size, with the strong potential to revolutionize the entire field.

Acknowledgments

The research leading to these results has partially received funding from the European Union's Horizon 2020 research and innovation program under Grant Agreement No. 731877 SOLUS: Smart Optical and Ultrasound diagnostics of breast cancer and under Grant Agreement No. 654148 Laserlab-Europe.

References

1. D. A. Boas et al., "Imaging the body with diffuse optical tomography," *IEEE Signal Process. Mag.* **18**, 57–75 (2001).
2. T. Durduran et al., "Diffuse optics for tissue monitoring and tomography," *Rep. Prog. Phys.* **73**, 076701 (2010).
3. H. Zhao et al., "Time-resolved diffuse optical tomography and its application to in vitro and in vivo imaging," *J. Biomed. Opt.* **12**, 062107 (2007).
4. A. T. Eggebrecht et al., "Mapping distributed brain function and networks with diffuse optical tomography," *Nat. Photonics* **8**, 448–454 (2014).
5. R. Choe et al., "Differentiation of benign and malignant breast tumors by in-vivo three-dimensional parallel-plate diffuse optical tomography," *J. Biomed. Opt.* **14**, 024020 (2009).
6. L. Di Sieno et al., "Toward noninvasive assessment of flap viability with time-resolved diffuse optical tomography: a preclinical test on rats," *J. Biomed. Opt.* **21**, 025004 (2016).
7. J. Steinbrink et al., "Determining changes in NIR absorption using a layered model of the human head," *Phys. Med. Biol.* **46**(3), 879–896 (2001).
8. J. Selb et al., "Improved sensitivity to cerebral hemodynamics during brain activation with a time-gated optical system: analytical model and experimental validation," *J. Biomed. Opt.* **10**, 011013 (2005).
9. L. Zucchelli et al., "Method for the discrimination of superficial and deep absorption variations by time domain fNIRS," *Biomed. Opt. Express* **4**, 2893–2910 (2013).
10. A. Puszka et al., "Spatial resolution in depth for time-resolved diffuse optical tomography using short source-detector separations," *Biomed. Opt. Express* **6**, 1–10 (2015).
11. L. Di Sieno et al., "Diffuse optics using a dual window fast-gated counter," *Appl. Opt.* **53**, 7394–7401 (2014).
12. F. Gao, H. Zhao, and Y. Yamada, "Improvement of image quality in diffuse optical tomography by use of full time-resolved data," *Appl. Opt.* **41**, 778–791 (2002).
13. A. Puszka et al., "Time-domain reflectance diffuse optical tomography with Mellin-Laplace transform for experimental detection and depth localization of a single absorbing inclusion," *Biomed. Opt. Express* **4**, 569–583 (2013).
14. A. Torricelli et al., "Time domain functional NIRS imaging for human brain mapping," *Neuroimage* **85**, 28–50 (2014).
15. A. Pifferi et al., "New frontiers in time domain diffuse optics," *J. Biomed. Opt.* **21**, 091310 (2016).
16. F. E. W. Schmidt et al., "A 32-channel time-resolved instrument for medical optical tomography," *Rev. Sci. Instrum.* **71**, 256 (2000).
17. R. J. Cooper et al., "MONSTIR II: A 32-channel, multispectral, time-resolved optical tomography system for neonatal brain imaging," *Rev. Sci. Instrum.* **85**, 053105 (2014).
18. H. Eda et al., "Multichannel time-resolved optical tomographic imaging system," *Rev. Sci. Instrum.* **70**, 3595–3602 (1999).
19. V. Ntziachristos et al., "Multichannel photon counting instrument for spatially resolved near infrared spectroscopy," *Rev. Sci. Instrum.* **70**, 193 (1999).
20. W. Becker, *The bh TCSPC Handbook*, 6th ed., Becker and Hickl (2015).
21. R. H. Hadfield, "Single-photon detectors for optical quantum information applications," *Nat. Photonics* **3**, 696–705 (2009).
22. A. Pifferi et al., "Time-resolved diffuse reflectance using small source-detector separation and fast single-photon gating," *Phys. Rev. Lett.* **100**, 138101 (2008).
23. L. Di Sieno et al., "Functional near-infrared spectroscopy at small source-detector distance by means of high dynamic-range fast-gated SPAD acquisitions: first *in-vivo* measurements," *Proc. SPIE* **8804**, 880402 (2013).
24. A. Dolgoshein et al., "Status report on silicon photomultiplier development and its applications," *Nucl. Instrum. Methods Phys. Res. Sect. A* **563**, 368–376 (2006).
25. A. Dalla Mora et al., "Towards next-generation time-domain diffuse optics for extreme depth penetration and sensitivity," *Biomed. Opt. Express* **6**, 1749–1760 (2015).
26. A. Dalla Mora et al., "Fast silicon photomultiplier improves signal harvesting and reduces complexity in time-domain diffuse optics," *Opt. Express* **23**, 13937–13946 (2015).
27. E. Martinenghi et al., "Time-resolved single-photon detection module based on silicon photomultiplier: a novel building block for time-correlated measurement systems," *Rev. Sci. Instrum.* **87**, 073101 (2016).
28. S. K. V. Sekar et al., "Broadband (600–1350 nm) time resolved diffuse optical spectrometer for clinical use," *IEEE J. Sel. Top. Quantum Electron.* **22**, 1–9 (2016).
29. S. Fujisaka et al., "A clinical tissue oximeter using NIR time-resolved spectroscopy," in *Proc. 43rd Annual Meeting of the Int. Society on Oxygen Transport to Tissue*, C. E. Elwell, T. S. Leung, and D. K. Harrison, Eds., Vol. **876**, pp. 427–234 (2016).
30. F. Villa et al., "Analog SiPM in planar CMOS technology," in *Proc. of Solid State Device Research Conf.*, pp. 294–297 (2014).
31. S. Mandai and E. Charbon, "Multi-channel digital SiPMs: concept, analysis and implementation," in *IEEE Nuclear Science Symp. and Medical Imaging Conf.*, pp. 1840–1844 (2012).
32. E. Martinenghi et al., "Spectrally-resolved single-photon timing of silicon photomultipliers for time-domain diffuse optics," *IEEE Photonics J.* **7**, 6802512 (2015).
33. D. Contini et al., "Effects of time-gated detection in diffuse optical imaging at short source-detector separation," *J. Phys. D: Appl. Phys.* **48**, 045401 (2015).
34. A. Puszka et al., "Time-resolved diffuse optical tomography using fast-gated single-photon avalanche diodes," *Biomed. Opt. Express* **4**, 1351–1365 (2013).
35. F. Martelli et al., "Phantoms for diffuse optical imaging based on totally absorbing objects, part 1: basic concepts," *J. Biomed. Opt.* **18**, 066014 (2013).
36. F. Martelli et al., "Phantoms for diffuse optical imaging based on totally absorbing objects, part 2: Experimental implementation," *J. Biomed. Opt.* **19**, 076011 (2014).

37. M. S. Patterson, B. Chance, and B. C. Wilson, "Time resolved reflectance and transmittance for the non-invasive measurement of tissue optical properties," *Appl. Opt.* **28**, 2331–2336 (1989).
38. L. Hervé et al., "Time-domain diffuse optical tomography processing by using the Mellin-Laplace transform," *Appl. Opt.* **51**, 5978–5988 (2012).
39. M. Fox, *Quantum Optics: An Introduction*, Oxford University Press, New York (2006).
40. G. Boso et al., "Fast-gating of single-photon avalanche diodes with 200 ps transitions and 30 ps timing jitter," *Sens. Actuators A* **191**, 61–67 (2013).
41. A. Bassi et al., "Temporal propagation of spatial information in turbid media," *Opt. Lett.* **33**, 2836–2838 (2008).
42. H. Dehghani et al., "Three-dimensional optical tomography: resolution in small-object imaging," *Appl. Opt.* **42**, 3117–3128 (2003).
43. J. Zouaoui et al., "Quantification in time-domain diffuse optical tomography using Mellin–Laplace transforms," *Biomed. Opt. Express* **7**, 4346–4363 (2016).

Laura Di Sieno received her master's degree in electronics engineering at the Politecnico di Milano, Italy, in 2011, and her PhD in physics at the same university in 2015. Since January 2015, she has been a postdoctoral fellow, and her activity is mainly focused on the study and application of instrumentation for time-resolved optical spectroscopy of highly scattering media using SPAD enabled in fast-gated mode.

Judy Zouaoui received her Engineer's degree in biomedical engineering in 2013 from the Engineering School of Polytech, Lyon, France. The same year, she obtained her master's degree in medical imaging from the University of Lyon 1 in France. Since November 2013, she has been a PhD student at CEA LETI and at the University Grenoble Alpes on the topic of multispectral time-resolved diffuse optical tomography.

Lionel Hervé has mainly worked on signal processing for medical imaging. He studied the relationship between mammographic densities and cancer occurrence on large population trials in a two-year postdoc fellowship in UCSF. Since 2005, he worked on the diffuse optical tomography modality which consists of reconstructing 3-D optical property maps from IR optical measurements. He particularly focused on the processing of time-domain optical measurements to probe deeper inside biological media.

Antonio Pifferi graduated in nuclear engineering in 1991 and received his PhD in physics in 1995 at the Politecnico di Milano. Since 2003, he has been an associate professor in the Physics Department of the Polytechnic of Milan. His research focuses on the development of new laser and instrumentation exploiting light propagation in highly scattering media with applications to optical characterization of biological tissues, optical mammography.

Andrea Farina received his master's degree (cum laude) in electronics engineering from Politecnico di Milano, Italy, in 2005, and his PhD degree in physics at the same institution in 2009. Since December 2011, he has held a permanent position as a researcher at the Italian National Research Council (CNR) in Milan. His current research includes the development and the application of time-resolved techniques for the imaging and spectral characterization of diffusive media.

Edoardo Martinenghi received his master's degree in electronics engineering from the Politecnico di Milano, Italy, in 2013, where he is currently working toward his PhD. Currently, his research activity concerns the design of TD diffuse spectroscopy instrumentations and their applications to biomedical diagnosis.

Jacques Derouard is a professor emeritus of physics at the University Grenoble Alpes. His current research interests are related to optics and spectroscopy methodologies applied to life sciences, more specifically fluorescence correlation spectroscopy and optics in turbid media.

Jean-Marc Dinten is a senior scientist at the Biology and Health Division in CEA-LETI. For more than 20 years, he has been widely developing medical image processing and reconstruction algorithms associated to the development of innovative x-rays and optical imaging systems. He now heads the Imaging Readout Systems Laboratory, which develops new optical imaging systems for health and biology applications.

Alberto Dalla Mora has been an assistant professor in the Department of Physics, Politecnico di Milano, Italy, since 2011. He graduated summa cum laude in electronics engineering from Politecnico di Milano in 2006, and he received his PhD degree summa cum laude in information and communication technology at the same university in 2010. He authored more than 35 papers in international peer-reviewed journals. Currently, his research interests include time-resolved diffuse spectroscopy instrumentation and applications for biomedical diagnosis.